Metasurface-Enabled Extremely Large-Scale Antenna Systems: Transceiver Architecture, Physical Modeling, and Channel Estimation

Zhengyu Wang, Student Member, IEEE, Tiebin Mi, Member, IEEE, Gui Zhou, Member, IEEE, Robert C. Qiu, Fellow, IEEE

Abstract—Extremely large-scale antenna arrays (ELAAs) have emerged as a pivotal technology for addressing the unprecedented performance demands of next-generation wireless communication systems. To enhance their practicality, we propose metasurfaceenabled extremely large-scale antenna (MELA) systems-novel transceiver architectures that employ reconfigurable transmissive metasurfaces to facilitate efficient over-the-air RF-to-antenna coupling and phase control. This architecture eliminates the need for bulky switch matrices and costly phase-shifter networks typically required in conventional solutions. Physically grounded models are developed to characterize electromagnetic field propagation through individual transmissive unit cells, capturing the fundamental physics of wave transformation and transmission. Additionally, distance-dependent approximate models are introduced, exhibiting structural properties conducive to efficient parameter estimation and signal processing. Based on the channel model, a two stage channel estimation framework is proposed for the scenarios comprising users in the hybrid nearand far-fields. In the first stage, a dictionary-driven beamspace filtering technique enables rapid angular-domain scanning. In the refinement stage, the rotational symmetry of subarrays is exploited to design super-resolution estimators that jointly recover angular and range parameters. An analytical expression for the half-power beamwidth of MELA is derived, revealing its near-optimal spatial resolution relative to conventional ELAA architectures. Numerical experiments further validate the highresolution of the proposed channel estimation algorithm and the fidelity of the electromagnetic model, positioning the MELA architecture as a highly competitive and forward-looking solution for practical ELAA deployment.

Index Terms—metasurfaces, ELAA, transceiver architecture, electromagnetic channel model, hybrid-field channel.

I. Introduction

The deployment of multiple antennas has long been a cornerstone in the evolution of wireless communications, enabling foundational technologies such as MIMO systems and spatial beamforming [1]–[3]. As the vision for sixthgeneration (6G) and next-generation wireless networks continues to evolve, extremely large-scale antenna arrays (ELAAs), also known as extremely large-scale multiple-input multiple-output (XL-MIMO), have emerged as a key enabler to meet the unprecedented demands for spectral efficiency [4], [5], spatial resolution [6], and massive user connectivity [7]. By

Z. Wang, T. Mi, G. Zhou and R. C. Qiu are with the School of Electronic Information and Communications (EIC), Huazhong University of Science and Technology (HUST), Wuhan 430074, China. (e-mail:wangzhengyu@hust.edu.cn; mitiebin@hust.edu.cn; gui.zhou@fau.de; caiming@hust.edu.cn).

This work is supported by the National Natural Science Foundation of China under Grant 12141107, the Key Research and Development Program of Wuhan under Grant 2024050702030100, and the Interdisciplinary Research Program of HUST (2023JCYJ012).

substantially increasing both the aperture size and the number of radiating elements, ELAAs introduce new spatial degrees of freedom that fundamentally transform the wireless interface.

One of the most critical and persistent challenges in the practical realization of ELAAs is the efficient interfacing of a massive number of antenna elements with a limited set of radio frequency (RF) chains [8]. While one-to-one RF-toantenna mapping remains marginally feasible in conventional massive MIMO systems, such direct connectivity becomes impractical at ELAA scales due to prohibitive hardware costs, excessive power consumption, and significant implementation complexity [9]. Moreover, the interconnection complexity and the required number of phase shifters scale with the product of the number of RF chains and the array size. As a compromise, partially connected architectures have been proposed, wherein a reduced number of RF chains are dynamically linked to the antenna array via networks of switches [10], [11], as illustrated in Fig. 1. Although these multiplexing schemes offer a more cost- and energy-efficient alternative to full connectivity, they still involve substantial hardware complexity and bulky circuitry, ultimately limiting the scalability of the system. These challenges may partly explain the current lack of large-scale ELAA hardware prototypes.

Recent advances in metasurface technologies [12] open new avenues for simplifying transceiver architectures by replacing conventional switch and phase-shifter networks with over-the-air transmission and reception. This paper proposes metasurface-enabled extremely large-scale antenna (MELA) systems—novel transceiver architectures designed to achieve scalable and hardware-efficient ELAAs. Unlike traditional wired implementations, MELA systems exploit the wireless channel for transceiver-to-antenna coupling and delegate phase control to the metasurface itself, as illustrated in Fig. 2, thereby eliminating the need for bulky switch matrices and costly phase-shifter networks. This architectural enables seamless expansion of both RF chains and antenna elements without requiring substantial modifications to the underlying design.

A. Contributions

The main contributions of this work are summarized as follows:

1) Transmissive metasurface-enabled over-the-air architecture: We propose a novel transceiver architecture for ELAAs that leverages reconfigurable transmissive metasurfaces. Unlike conventional ELAA systems that rely on dense networks of switches and phase shifters, the proposed MELA architecture utilizes the wireless channel for transceiver-to-antenna coupling and delegates phase control

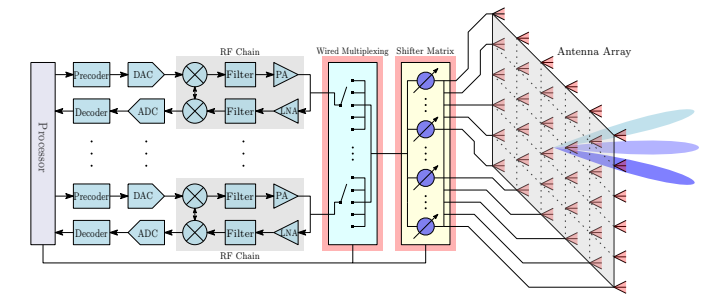


Fig. 1: Illustration of the ELAA architecture, where high-overhead switches and phase shifters dynamically manage the connections between a limited number of RF chains and the full antenna array.

to the metasurface. This over-the-air design substantially reduces hardware complexity, cost, and signal routing overhead, thereby advancing the practical implementation of ELAA systems.

- 2) Physically interpretable and mathematically tractable channel modeling for MELA: We propose a theoretical framework to accurately model the end-to-end wireless link-from the source to the transmissive metasurface and finally to the receiver aperture—as a cascaded interaction of electromagnetic fields. We obtain closed-form expressions for the electric field and establish a matrix-form channel representation. Based on the placement distances between the metasurface and receivers, we further derive distance-specific approximate channel models that not only offer accurate characterization but also exhibit desirable structural properties for efficient analysis and processing.
- 3) Hybrid-field and gridless channel estimation for MELA: We propose a two-stage uplink channel estimation framework which supports both near- and far-field signal components. In the coarse stage, a dictionary-driven beamspace filtering technique enables fast angular domain scanning via dynamic phase configuration of the metasurface. In the refinement stage, we exploit the subarray rotational symmetry to construct super-resolution estimators that jointly recover angle and distance parameters. Furthermore, we derive the half-power beamwidth (HPBW) expression for the MELA system and show that its spatial resolution closely approximates that of traditional ELAA architectures under practical conditions, validating its effectiveness for high-precision sensing and channel acquisition.

B. Prior Works

1) Hardware Architecture: The concept of reconfigurable transmitarrays was initially introduced in [13], where the authors proposed a sandwich-structured planar three-dimensional lens. This architecture comprises a receiving antenna array phase-coupled to a transmitting array via tunable phase shifters, jointly illuminated by one or multiple focal sources [14], [15]. In a recent implementation, Cui et al. [16] developed a hybrid architecture combining a metasurface lens with a programmable uniform linear feed array positioned along the lens's focal line.

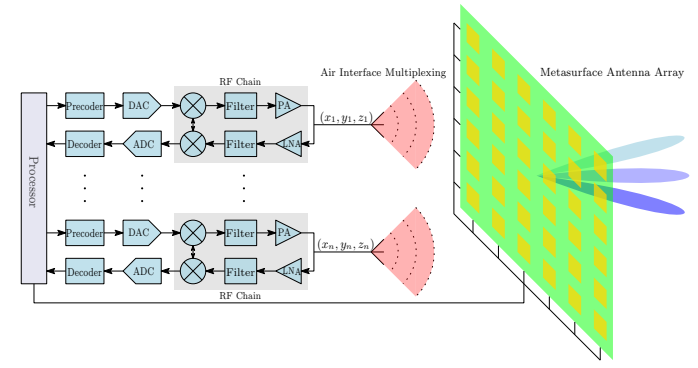


Fig. 2: Illustration of the MELA architecture, which employs over-the-air transceiver-to-antenna coupling and delegates phase control to the reconfigurable metasurface.

- 2) Theoretical Modeling: In theoretical research, the structure of a reconfigurable metasurface integrated with a feed antenna was employed in [17]–[19] for signal modulation and downlink wireless transmission. However, these studies share a critical limitation: the wireless channel between the feed antenna and the metasurface is often ignored, and the transmitter is modeled as a unified black-box entity. Subsequently, [20] established transmission schemes for both downlink and uplink communications under this architecture. For uplink systems, [21] proposed a joint optimization framework that simultaneously adjusts power allocation and the phase-shift coefficients of the transmissive metasurface to maximize the system sum-rate, and [22] investigated this transceiver architecture in cell-free massive MIMO uplink scenarios. These studies commonly assume that the distance between the transmissive metasurface and the receiver lies within the Rayleigh zone, where the metasurface-receiver link can be characterized by a line-of-sight near-field propagation model [20]-[22]. However, in the sub-aperture near-field region-as experimentally validated in [20]—the physical dimensions of the antenna elements become non-negligible. Prior works model each antenna element as a point source, which renders conventional channel models insufficient for precisely characterizing the behavior of reconfigurable transmitarrays in this regime.
- Channel Estimation: As the Fresnel region significantly expands in ELAA system, and signal sources may reside in either the near-field or far-field regime [23]. When both near-field and far-field signals coexist, near-field steering vectors introduce energy spreading along the distance dimension for far-field signals, while far-field steering vectors cause angular-domain leakage for near-field signals [24]. These power diffusion effects [25] pose major challenges to conventional channel estimation methods, which typically assume a single-field scenario. Moreover, due to the inherent non-orthogonality of near-field steering vectors [26], conventional sparse recovery algorithms such as orthogonal matching pursuit (OMP) in the polar domain [27] become ineffective. To address this, several recent studies have proposed novel hybrid-field sparse channel representations [28], [29] . Beyond compressed sensing, [30] exploits array geometry symmetry and employs a modified MUSIC

algorithm to decouple angle and distance estimation [31]. However, the iterative scheme in [29] incurs substantial computational overhead, while the spectral search methods in [30], [31] suffer from large search spaces and high complexity. Additionally, sparse-based hybrid channel estimation approaches face fundamental limitations, including grid mismatch errors that constrain estimation accuracy and the use of excessively dense grids that increase dictionary size. Despite these advances, high-dimensional channel estimation in ELAA systems remains a critical and open research challenge.

The remainder of this paper is organized as follows. In Section II, the MELA architecture and corresponding channel models are introduced. In Section III, we present a channel estimation scheme specifically designed for the MELA architecture. In Section IV, we derive an expression for HPBW of the MELA and compare its spatial resolution with that of conventional ELAA architectures. Simulation results are provided in Section V. Finally, Section VI concludes the paper.

Notations: Upper-case and lower-case boldface letters denote matrices and column vectors, respectively. The operators $(\cdot)^T$, $(\cdot)^*$, and $(\cdot)^H$ denote the transpose, conjugate, and Hermitian transpose, respectively. We use $\|\cdot\|$ to denote the Euclidean norm for vectors. diag(\mathbf{a}) returns a diagonal matrix with the elements in \mathbf{a} as its main diagonal entries. Additionally, \mathbf{I}_n denotes $n \times n$ identity matrix and \odot represents the Hadamard matrix product. For a complex number z, we use mag(z) and arg(z) to represent the magnitude and the argument of z respectively. We use $z \sim \mathcal{CN}(m, \sigma^2)$ for a complex circular Gaussian distribution with mean m and variance σ^2 .

II. TRANSCEIVER ARCHITECTURE AND THEORETICAL MODELING

Unlike conventional wired interfacing schemes that multiplex each RF chain to antenna elements using switch networks and physical connections, the MELA system introduces an over-the-air interface between RF chains and the antenna array, as illustrated in Fig. 2. Specifically, MELA employs passive transmissive metasurfaces to relay and multiplex signals to and from sources. To realize the wireless coupling mechanism, auxiliary feed antennas are deployed at the RF end to illuminate the metasurface.

We consider the topology configuration in which the transmissive metasurface lies in the zoy-plane, with the center of the metasurface array positioned at the origin of the coordinate system. The metasurface consists of $N = (2N_h + 1) \times (2N_v + 1)$ unit cells, uniformly spaced by a distance d in both the horizontal and vertical directions. Assume that there are M antennas at the receiver side, and K sources located at positions $\mathbf{p}_1, \ldots, \mathbf{p}_K$. For simplicity, sources are modeled as infinitesimal dipole antennas aligned along the z-axis. Although infinitesimal dipoles are not physically realizable, they are widely used to approximate short electric dipoles. Assume a line-of-sight (LoS) path between the source and the metasurface. Without loss of generality, we illustrate the modeling approach by focusing on the electromagnetic characteristics of the uplink channel and analyzing the k-th

source-induced power at the m-th receiving element through n-th transmissive unit cell. Under this setting, the electric field at an observation point $\bar{\mathbf{t}}_n$ on the transmissive unit cell can be expressed as

$$\mathbf{E}(\bar{\mathbf{t}}_n) = \frac{I_0 l \eta}{4\pi} \frac{e^{jk_c \|\mathbf{p}_k - \bar{\mathbf{t}}_n\|}}{\|\mathbf{p}_k - \bar{\mathbf{t}}_n\|} \mathbf{e}_{\theta}.$$
 (1)

Here l is the length of the dipole antenna, η is the intrinsic impedance of the medium, I_0 is the current amplitude, and $k_c = 2\pi/\lambda$ is the wavenumber. The unit vector \mathbf{e}_{θ} , representing the elevation direction in spherical coordinates, is expressed in Cartesian coordinates as $\mathbf{e}_{\theta} = (\mathbf{e}_z \times \mathbf{R}_t) \times \mathbf{R}_t$ where \mathbf{e}_z is the unit vector along the z-axis, and \mathbf{R}_t is the unit vector pointing from the source to the observation point, defined as $\mathbf{R}_t = (\mathbf{p}_k - \bar{\mathbf{t}}_n)/\|\mathbf{p}_k - \bar{\mathbf{t}}_n\|$. Under the same setting, the incident magnetic field at $\bar{\mathbf{t}}_n$ is given by

$$\mathbf{H}^{i} = \frac{1}{\eta} \mathbf{R}_{t} \times \mathbf{E}(\bar{\mathbf{t}}_{n}) = \frac{I_{0}l}{4\pi} \frac{e^{jk_{c} \|\mathbf{p}_{k} - \bar{\mathbf{t}}_{n}\|}}{\|\mathbf{p}_{k} - \bar{\mathbf{t}}_{n}\|} \mathbf{e}_{\phi}, \tag{2}$$

where $\mathbf{e}_{\phi} = \mathbf{e}_z \times \mathbf{R}_t$ is the azimuthal unit vector in the spherical coordinate system.

For transmissive metasurfaces, the receive-to-radiate operation is the fundamental working principle. Let the transmission coefficient of a unit cell be denoted by Γ . Then, the transmitted magnetic field can be expressed as $\mathbf{H}^t = \Gamma \mathbf{H}^i$, where \mathbf{H}^i is the incident magnetic field. Neglecting edge effects due to the finite aperture size and applying the surface equivalence principle, each unit cell can be modeled as an equivalent surface current source. Accordingly, the equivalent surface current density is given by

$$\mathcal{J}(\bar{\mathbf{t}}_n) = \hat{\mathbf{n}} \times (\mathbf{H}^i + \mathbf{H}^t) = (1 + \Gamma)\mathbf{e}_x \times \mathbf{H}^i$$

$$= \frac{(1 + \Gamma)I_0l}{4\pi} \frac{e^{jk_c \|\mathbf{p}_k - \bar{\mathbf{t}}_n\|}}{\|\mathbf{p}_k - \bar{\mathbf{t}}_n\|} \cos \phi_{nk} \, \mathbf{e}_z, \qquad (3)$$

where ϕ_{nk} is the angle between the projection of \mathbf{R}_t onto the xy-plane and the positive x-axis.

Unlike conventional architectures that rely on centralized phase shifter networks, a distinguishing feature of MELA is that phase shifting is implemented directly at the unit-cell level. This introduces an additional phase modulation term in the equivalent surface current density. As a result, the electric field at $\bar{\mathbf{r}}_m$ on the m-th receiving element due to radiation transmitted through the n-th unit cell can be formulated as

$$\mathbf{E}_{r} = \frac{j\eta}{4\pi k_{c}} \int_{S_{r}} \int_{S_{t}} \frac{e^{j\omega_{n}} \mathcal{J}(\bar{\mathbf{t}}_{n}) e^{jk_{c} \|\bar{\mathbf{t}}_{n} - \bar{\mathbf{r}}_{m}\|}}{\|\bar{\mathbf{t}}_{n} - \bar{\mathbf{r}}_{m}\|} d\bar{\mathbf{t}}_{n} d\bar{\mathbf{r}}_{m}, \quad (4)$$

where S_t and S_r denote the surface areas of of the n-th transmissive unit cell and the m-th receiving unit, respectively. The coordinates of any point on the transmissive unit cell can be expressed as the sum of the unit cell center position \mathbf{t}_n and a local offset vector $\Delta \mathbf{t}_n$ that represents the displacement from the center (a similar decomposition applies to $\bar{\mathbf{r}}_m$)

$$\bar{\mathbf{t}}_n = \mathbf{t}_n + \Delta \mathbf{t}_n, \bar{\mathbf{r}}_m = \mathbf{r}_m + \Delta \mathbf{r}_m.$$

When the physical dimensions of both the transmissive unit cell and the receiving aperture are small relative to their separation distance, the expression in (4) can be significantly

$$\mathbf{E}_{r} = \frac{I_{0}l\eta}{4\pi k_{c}} \frac{j(1+\Gamma)}{4\pi} \frac{e^{jk_{c}\|\mathbf{d}_{mn}\|} e^{jk_{c}\|\mathbf{p}_{k} - \bar{\mathbf{t}}_{n}\|}}{\|\mathbf{d}_{mn}\|\|\mathbf{p}_{k} - \bar{\mathbf{t}}_{n}\|} \int_{S_{t}} e^{jk_{c}(\frac{\mathbf{d}_{mn}}{\|\mathbf{d}_{mn}\|} - \frac{\mathbf{p} - \bar{\mathbf{t}}_{n}}{\|\mathbf{p} - \bar{\mathbf{t}}_{n}\|})^{\mathsf{T}} \Delta \mathbf{t}_{n}} d\Delta \mathbf{t}_{n} \int_{S_{r}} e^{-jk_{c} \frac{\mathbf{d}_{mn}^{\mathsf{T}} \Delta \mathbf{r}_{m}}{\|\mathbf{d}_{mn}\|}} d\Delta \mathbf{r}_{m} \cos \phi_{nk} e^{j\omega_{n}} \mathbf{e}_{z}.$$
(7)

simplified. Specifically, we denote $\mathbf{d}_{mn} = \mathbf{t}_n - \mathbf{r}_m$ the vector from the center of the *n*-th transmissive unit cell to the center of the *m*-th receiving aperture. Under the approximation, the distance in the denominator can be approximated as follows

$$\frac{e^{jk_{c}\|\bar{\mathbf{t}}_{n}-\bar{\mathbf{r}}_{m}\|}}{\|\bar{\mathbf{t}}_{n}-\bar{\mathbf{r}}_{m}\|} \approx \frac{e^{jk_{c}\|\mathbf{d}_{mn}+\Delta\mathbf{t}_{n}-\Delta\mathbf{r}_{m}\|}}{\|\mathbf{d}_{mn}\|},$$

$$\frac{e^{jk_{c}\|\mathbf{p}_{k}-\bar{\mathbf{t}}_{n}\|}}{\|\mathbf{p}_{k}-\bar{\mathbf{t}}_{n}\|} \approx \frac{e^{jk_{c}\|\mathbf{p}_{k}-\mathbf{t}_{n}-\Delta\mathbf{t}_{n}\|}}{\|\mathbf{p}_{k}-\mathbf{t}_{n}\|}.$$
(5)

We then focus on the exponential phase terms, where the Euclidean distances in the exponentials can be further approximated using first-order Taylor expansion as follows

$$\|\mathbf{d}_{mn} + \Delta \mathbf{t}_{n} - \Delta \mathbf{r}_{m}\| \approx \|\mathbf{d}_{mn}\| + \frac{\mathbf{d}_{mn}^{\mathsf{T}}(\Delta \mathbf{t}_{n} - \Delta \mathbf{r}_{m})}{\|\mathbf{d}_{mn}\|},$$

$$\|\mathbf{p}_{k} - \mathbf{t}_{n} - \Delta \mathbf{t}_{n}\| \approx \|\mathbf{p}_{k} - \mathbf{t}_{n}\| - \frac{(\mathbf{p}_{k} - \mathbf{t}_{n})^{\mathsf{T}} \Delta \mathbf{t}_{n}}{\|\mathbf{p}_{k} - \mathbf{t}_{n}\|}.$$
(6)

By substituting the approximations in (5) and (6) into the integral expression in (4), we obtain the simplified formulation presented in (7). Furthermore, if the apertures have regular and analytically tractable geometries, such as squares, the expression can be further simplified, leading to the following theorem.

Theorem 1. Suppose that both the receiving antenna and the transmissive unit cell have square apertures with side lengths d_r and d_t . Then, the amplitude of the resulting electric field at the m-th receiving antenna, due to a source located at position \mathbf{p}_k , is given by

$$\mathbf{E}_{r} = \mathcal{A}_{mn} \mathcal{B}_{nk} \frac{e^{jk_{c}\|\mathbf{d}_{mn}\|} e^{jk_{c}\|\mathbf{p}_{k} - \mathbf{t}_{n}\|}}{\|\mathbf{d}_{mn}\|\|\mathbf{p}_{k} - \mathbf{t}_{n}\|} e^{j\omega_{n}} I_{0} l \eta, \qquad (8)$$

where the scalars A_{mn} and B_{nk} are defined as

$$\begin{split} \mathcal{A}_{mn} &= \frac{j d_r^2}{4\pi k_c} \cdot \operatorname{sinc}\left(\frac{k_c v_y d_r}{2}\right) \operatorname{sinc}\left(\frac{k_c v_z d_r}{2}\right), \\ \mathcal{B}_{nk} &= \frac{(1+\Gamma) d_t^2}{4\pi} \cdot \operatorname{sinc}\left(\frac{k_c u_y d_t}{2}\right) \operatorname{sinc}\left(\frac{k_c u_z d_t}{2}\right) \cos\phi_{nk}. \end{split}$$

The normalized direction vectors ${\bf u}$ and ${\bf v}$ are defined as

$$\mathbf{v} = \mathbf{d}_{mn}/\|\mathbf{d}_{mn}\| = [v_x, v_y, v_z]^\mathsf{T},$$

$$\mathbf{u} = \mathbf{p}_k - \mathbf{t}_n/\|\mathbf{p}_k - \mathbf{t}_n\| + \mathbf{d}_{cn}/\|\mathbf{d}_{cn}\| = [u_x, u_y, u_z]^\mathsf{T}.$$

Proof. Please refer to Section A of the appendix. \Box

Theorem 1 derives a closed-form expression for the amplitude of the electric field at the receiving element. The sinc functions in \mathcal{A}_{mn} and \mathcal{B}_{nk} represent the directional responses of the receiving apertures and the transmissive unit cells, respectively. When $d_r \ll \lambda$ or $d_t \ll \lambda$, the corresponding sinc terms approach unity, implying that the receiving aperture or the transmissive unit cell behaves approximately as an ideal isotropic radiator. To construct the complete signal propagation model, we invoke the principle of linear superposition to aggregate contributions from all unit cells. This leads to the

following matrix-form expression for the amplitude of the received electric field.

Corollary 1. Assume there are K sources with infinitesimal dipole antennas, and consider a digital decoding architecture with N_s RF chains connected to M receiver antennas. Let $\mathbf{H} \in \mathbb{C}^{M \times N}$ denote the channel matrix characterizing the propagation from the transmissive metasurface to the receiving antennas, with each element given by

$$\mathbf{H}_{mn} = \mathcal{A}_{mn} e^{jk_c \|\mathbf{d}_{mn}\|} / \|\mathbf{d}_{mn}\|, \tag{9}$$

and let $\mathbf{G} \in \mathbb{C}^{N \times K}$ model the propagation from the sources to the transmissive metasurface, where the k-th column is given by

$$\mathbf{G}_{:,k} = \left[\frac{\mathcal{B}_{1k} e^{jk_c \|\mathbf{p}_k - \mathbf{t}_1\|}}{\|\mathbf{p}_k - \mathbf{t}_1\|}, \dots, \frac{\mathcal{B}_{Nk} e^{jk_c \|\mathbf{p}_k - \mathbf{t}_N\|}}{\|\mathbf{p}_k - \mathbf{t}_N\|} \right]^{\mathsf{T}}. \quad (10)$$

Under this architecture, the received signal is given by

$$\mathbf{y} = \mathbf{F}_{BB}^{\mathsf{H}} \mathbf{H} \mathbf{\Phi} \mathbf{G} \mathbf{s} + \mathbf{n}, \tag{11}$$

where $\mathbf{s} = [(I_0)_1 l_1 \eta, \dots, (I_0)_K l_K \eta]^\mathsf{T}$ denotes the transmitted signal vector, $\mathbf{F}_{BB}^\mathsf{H} \in \mathbb{C}^{N_s \times M}$ is the baseband digital decoding matrix, and $\mathbf{n} \sim \mathcal{CN}(0, \sigma^2 \mathbf{I}_M)$ is the addictive white Gaussian noise vector with σ the power of the noise. The diagonal matrix $\mathbf{\Phi} = \mathrm{diag}(\boldsymbol{\omega}) \in \mathbb{C}^{N \times N}$ represents the phase configuration of the transmissive unit cells, where $\boldsymbol{\omega} = [e^{j\omega_1}, \dots, e^{j\omega_N}]$ contains the unit-modulus phase shifts.

Corollary 1 provides a physically interpretable and mathematically tractable formulation that explicitly captures the effects of spatial geometry, phase configuration, and wave propagation. The channel matrices **H** and **G** characterize the amplitude attenuation and phase delay along the paths from the sources and receivers to the transmissive unit cells. Notably, these matrices exhibit well-defined structures under certain geometric or operational conditions.

A. Co-located receiving apertures

We consider the scenario where the receiving antennas are co-located or closely spaced within a confined region. In this case, the distance $\|\mathbf{d}_{mn}\|$ in the exponential term can be further approximated using a second-order expansion around the array center, due to the limited spatial variation across the receiving elements. Specifically, the position vector of the m-th antenna element can be written as

$$\mathbf{r}_m = \mathbf{d}_c + \boldsymbol{\delta}_m,\tag{12}$$

where \mathbf{d}_c represents the geometric center of the receiving array, and δ_m denotes the relative displacement from \mathbf{d}_c to the m-th element, as illustrated in Fig. 3. Substituting (12) into $\|\mathbf{d}_{mn}\|$ and using the second order Taylor expansion, the expression of $\|\mathbf{d}_{mn}\|$ can be approximated as

$$\|\mathbf{d}_{mn}\| \approx \|\mathbf{d}_c\| - \frac{\mathbf{d}_c^\mathsf{T}(\mathbf{t}_n - \boldsymbol{\delta}_m)}{\|\mathbf{d}_c\|} + \frac{(\mathbf{t}_n - \boldsymbol{\delta}_m)^\mathsf{T}\mathcal{H}(\mathbf{t}_n - \boldsymbol{\delta}_m)}{2}$$
 (13)

$$= \|\mathbf{d}_c\| - \frac{\mathbf{d}_c^{\mathsf{T}}(\mathbf{t}_n - \boldsymbol{\delta}_m)}{\|\mathbf{d}_c\|} + \frac{\boldsymbol{\delta}_m^{\mathsf{T}} \mathcal{H} \boldsymbol{\delta}_m + \mathbf{t}_n^{\mathsf{T}} \mathcal{H} \mathbf{t}_n}{2} - \mathbf{t}_n^{\mathsf{T}} \mathcal{H} \boldsymbol{\delta}_m, \quad (14)$$

where \mathcal{H} denotes the Hessian matrix given by $\mathcal{H} = (\|\mathbf{d}_c\|^2 \mathbf{I} - \mathbf{d}_c \mathbf{d}_c^\mathsf{T}) / \|\mathbf{d}_c\|^3$. Similarly, the following approximations hold

$$\|\mathbf{d}_c + \boldsymbol{\delta}_m\| = \|\mathbf{d}_c\| + \mathbf{d}_c^{\mathsf{T}} \boldsymbol{\delta}_m / \|\mathbf{d}_c\| + \frac{\boldsymbol{\delta}_m^{\mathsf{T}} \mathcal{H} \boldsymbol{\delta}_m}{2} + o(\|\boldsymbol{\delta}_m\|^2),$$

$$\|\mathbf{d}_c - \mathbf{t}_n\| = \|\mathbf{d}_c\| - \mathbf{d}_c^{\mathsf{T}} \mathbf{t}_n / \|\mathbf{d}_c\| + \frac{\mathbf{t}_n^{\mathsf{T}} \mathcal{H} \mathbf{t}_n}{2} + o(\|\mathbf{t}_n\|^2).$$

Neglecting higher-order terms, the expression in (13) can be rewritten as

$$\|\mathbf{d}_{mn}\| \approx \|\mathbf{d}_c + \boldsymbol{\delta}_m\| + \|\mathbf{d}_c - \mathbf{t}_n\| - \|\mathbf{d}_c\| - \mathbf{t}_n^\mathsf{T} \mathcal{H} \boldsymbol{\delta}_m.$$
 (15)

Comparing (13) and (15), we observe that, unlike the original non-negative quadratic form in (13), the bilinear cross term in (15) generally has smaller magnitude and may even vanish, thus introducing only a minor perturbation to the overall approximation. When the receiving antennas are colocated within a confined region such that the cross term $\mathbf{t}_n^{\mathsf{T}} \mathcal{H} \boldsymbol{\delta}_m$ is sufficiently small, the distance term $\|\mathbf{d}_{mn}\|$ can be approximated as

$$\|\mathbf{d}_{mn}\| \approx \|\mathbf{d}_c + \boldsymbol{\delta}_m\| + \|\mathbf{d}_c - \mathbf{t}_n\| - \|\mathbf{d}_c\|.$$
 (16)

We refer to this quantity as the approximately decoupled distance, as it separates the contributions of the receiver and transmissive unit cell geometries relative to their respective array centers.

To further elucidate the condition under which the decoupling approximation holds, we examine a special case where the receiving antenna array is configured as a uniform linear array aligned along the y-axis and located in the z=0 plane. In this setting, the maximum phase discrepancy between the full distance expression in (13) and its decoupled approximation in (16) is bounded by

$$\left| \frac{2\pi}{\lambda} \left(\frac{\mathbf{t}_n^\mathsf{T} \boldsymbol{\delta}_m}{\|\mathbf{d}_c\|} - \frac{\mathbf{t}_n^\mathsf{T} \mathbf{d}_c \mathbf{d}_c^\mathsf{T} \boldsymbol{\delta}_m}{\|\mathbf{d}_c\|^3} \right) \right| \le \frac{2\pi D_1 D_h}{\lambda \|\mathbf{d}_c\|} \le \epsilon, \tag{17}$$

where D_1 denotes the maximum aperture diameter of the receiving array, $D_h = (2N_h + 1)d$ represents the physical apertures of the metasurface along the horizontal axes, and ϵ is the prescribed phase error tolerance. This phase discrepancy attains its maximum when $\mathbf{t}_n = [0, D_h/2, 0]^\mathsf{T}$ and $\boldsymbol{\delta}_m = [0, D_1/2, 0]^\mathsf{T}$. The corresponding minimum distance required to ensure the approximation remains within the specified error bound is given by

$$R_{\epsilon}^{d} = \frac{2\pi D_{1} D_{h}}{\lambda \epsilon}.$$
 (18)

Thus, when $\|\mathbf{d}_c\| > R_{\epsilon}^d$, the approximation error becomes negligible. For instance, by choosing $\epsilon = \pi/8$, we obtain $R_{\epsilon}^d = 4D_1D_h/\lambda$.

With the decoupled distance approximation in (16), the phase term $e^{jk_c\|\mathbf{d}_{mn}\|}$ can be decomposed into separable contributions from the receiver and the transmissive metasurface. Accordingly, each entry of the channel matrix \mathbf{H} can be written as

$$\mathbf{H}_{mn} = \mathcal{A}_{mn} e^{-jk_c \|\mathbf{d}_c\|} e^{jk_c \|\mathbf{d}_c + \boldsymbol{\delta}_m\|} e^{jk_c \|\mathbf{d}_c - \mathbf{t}_n\|} / \|\mathbf{d}_{mn}\|.$$

This yields the following factorized form

$$\mathbf{H} = \operatorname{diag}(\mathbf{h}_r)\mathbf{C}\operatorname{diag}(\mathbf{h}_t),\tag{19}$$

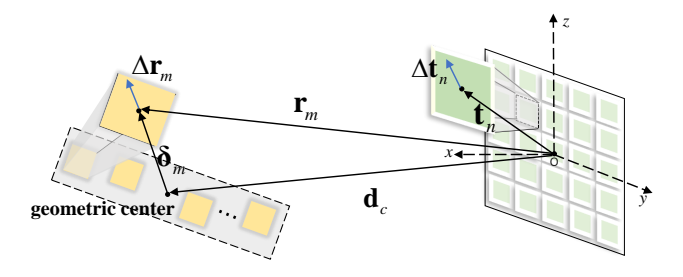


Fig. 3: Diagram of the transceiver architecture with receiving antennas confined to a localized region.

where the diagonal matrices $\operatorname{diag}(\mathbf{h}_r)$ and $\operatorname{diag}(\mathbf{h}_t)$ characterize the spatial phase responses at the receiver and transmissive metasurface sides, respectively, and the matrix \mathbf{C} represents amplitude attenuation. The components are defined as

$$\mathbf{h}_{r} = [e^{jk_{c}\|\mathbf{d}_{c} + \boldsymbol{\delta}_{1}\|}, \dots, e^{jk_{c}\|\mathbf{d}_{c} + \boldsymbol{\delta}_{M}\|}]^{\mathsf{T}},$$

$$\mathbf{h}_{t} = [e^{jk_{c}\|\mathbf{d}_{c} - \mathbf{t}_{1}\|}, \dots, e^{jk_{c}\|\mathbf{d}_{c} - \mathbf{t}_{N}\|}]^{\mathsf{T}},$$

$$[\mathbf{C}]_{mn} = \mathcal{A}_{mn}e^{-jk_{c}\|\mathbf{d}_{c}\|}/\|\mathbf{d}_{mn}\|.$$

Furthermore, if the non-negative quadratic form in (13) can be neglected, such as when $\|\mathbf{t}_n - \boldsymbol{\delta}_m\|$ is sufficiently small relative to the distance $\|\mathbf{d}_c\|$, the distance approximation simplifies considerably. In this regime, the second-order effects associated with array geometries become negligible, and the path length $\|\mathbf{d}_{mn}\|$ is dominated by the linear terms and we have

$$\|\mathbf{d}_{mn}\| \approx \|\mathbf{d}_c\| - \mathbf{d}_c^{\mathsf{T}}(\mathbf{t}_n - \boldsymbol{\delta}_m) / \|\mathbf{d}_c\|.$$
 (20)

We evaluate the accuracy of the linear approximation by quantifying the phase discrepancy introduced by the difference between the expression in (13) and its linearized counterpart in (20). Similar to the previous discussion, and assuming the receiving antenna array is configured as a uniform linear array, the resulting phase error is bounded by

$$\left| \frac{2\pi}{\lambda} \frac{(\mathbf{t}_n - \boldsymbol{\delta}_m)^\mathsf{T} \mathcal{H}(\mathbf{t}_n - \boldsymbol{\delta}_m)}{2} \right| \le \frac{\pi ((D_h + D_1)^2 + D_v^2)}{4\lambda \|\mathbf{d}_c\|} \le \epsilon, \quad (21)$$

where ϵ denotes the prescribed phase error tolerance. This leads to the following minimum distance requirement to ensure the validity of the linear approximation

$$R_{\epsilon}^{l} = \frac{\pi((D_h + D_1)^2 + D_v^2)}{4\lambda\epsilon},$$
 (22)

where $D_v=(2N_v+1)d$ represents the physical apertures of the metasurface along the vertical axes. When $\|\mathbf{d}_c\|\geq R_\epsilon^l$, the approximation error becomes negligible. Comparing the bounds in (18) and (22), we observe that the minimum distance required for the validity of the decoupled approximation R_ϵ^d , is generally more stringent than that for the linear approximation, R_ϵ^l , as shown in Fig. 4. This indicates that the decoupled model remains accurate across a wider range of practical configurations, while the linear model demands a stricter condition to limit the phase error within ϵ . For example, by choosing $\epsilon=\pi/8$, we have $R_\epsilon^l=2((D_h+D_1)^2+D_v^2)/\lambda$, which clearly exceeds R_ϵ^d .

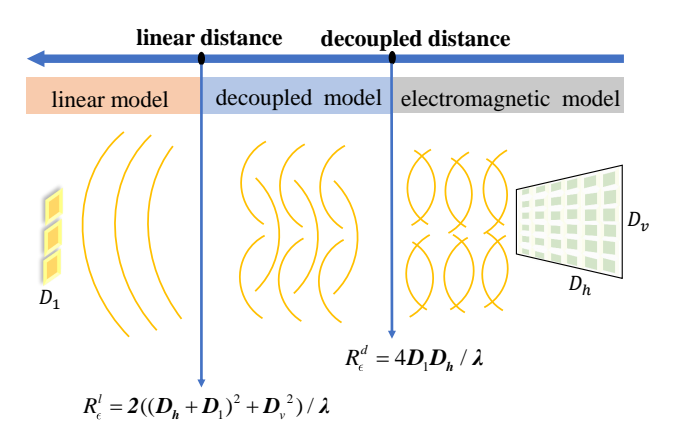


Fig. 4: Illustration of different modeling regimes based on the metasurface-receiver distance.

With the distance approximation in (20), the channel matrix **H** admits a significantly simplified form

$$\mathbf{H} = \mathcal{A}_c / \|\mathbf{d}_c\| \cdot \mathbf{h}_M \mathbf{h}_N^\mathsf{T},\tag{23}$$

where A_c denotes the attenuation coefficient, given by

$$\mathcal{A}_c = \frac{jd_r^2}{4\pi k_c} \cdot \operatorname{sinc}\left(\frac{k_c d_r}{2} \frac{[\mathbf{d}_c]_y}{\|\mathbf{d}_c\|}\right) \operatorname{sinc}\left(\frac{k_c d_r}{2} \frac{[\mathbf{d}_c]_z}{\|\mathbf{d}_c\|}\right),\,$$

and \mathbf{h}_M and \mathbf{h}_N are the steering vectors defined as

$$\mathbf{h}_{M} = [e^{jk_{c}\mathbf{d}_{c}^{\mathsf{T}}\boldsymbol{\delta}_{1}/\|\mathbf{d}_{c}\|}, \dots, e^{jk_{c}\mathbf{d}_{c}^{\mathsf{T}}\boldsymbol{\delta}_{M}/\|\mathbf{d}_{c}\|}],$$

$$\mathbf{h}_{N} = [e^{-jk_{c}\mathbf{d}_{c}^{\mathsf{T}}\mathbf{t}_{1}/\|\mathbf{d}_{c}\|}, \dots, e^{-jk_{c}\mathbf{d}_{c}^{\mathsf{T}}\mathbf{t}_{N}/\|\mathbf{d}_{c}\|}].$$

Consider a practical MELA system operating at a carrier frequency of 60 GHz, corresponding to a wavelength of 0.5 cm. The metasurface consists of 21×21 elements, and the receiver array contains 15 elements, with both having a unit spacing of half-wavelength. Consequently, the physical aperture of the receiver array is 3.75 cm, and the horizontal and vertical apertures of the metasurface are both 5.25 cm. Under this configuration, by choosing $\epsilon = \pi/8$, the values of R_ϵ^d and R_ϵ^l are 1.58 m and 4.34 m, respectively.

III. CHANNEL ESTIMATION

In this section, we focus on uplink channel estimation of the MELA system, which is a necessary step for subsequent analog/digital precoding in conventional communication pipelines. We consider a hybrid-field scenario where some sources reside in the near-field region, while others are in the far-field.

Assuming that sources are located at a moderately close distance to the metasurface, the phase across the unit cell varies significantly, yet the wavefront amplitude remains approximately uniform [32]. Under this assumption, the k-column of the matrix \mathbf{G} can be expressed as

$$\mathbf{G}_{:,k} = \left[\frac{\mathcal{B}_k}{\|\mathbf{p}_k\|} e^{jk_c\|\mathbf{p}_k - \mathbf{t}_1\|}, \dots, \frac{\mathcal{B}_k}{\|\mathbf{p}_k\|} e^{jk_c\|\mathbf{p}_k - \mathbf{t}_1\|} \right]^{\mathsf{T}},$$

where the subscript n in coefficient \mathcal{B}_{nk} is omitted since the amplitude variation across array elements is negligible. We represent the position coordinate of the k-th source as $\mathbf{p}_k = r_k [\sqrt{\cos^2\phi_k - \sin^2\theta_k}, \sin\theta_k, \sin\phi_k]^\mathsf{T}$, where θ_k and ϕ_k denote the source's azimuth and elevation angles relative to the center of the metasurface, respectively. Here, the elevation angle is defined as the angle between the source and the xoy plane, while the azimuth angle refers to the angle between the source and the xoz plane. The coordinates of the (n_y, n_z) -th element on the metasurface are given by $[0, n_yd, n_zd]^\mathsf{T}$. Substituting coordinates, the matrix \mathbf{G} can be expressed in terms of spherical wave steering vectors as

$$\mathbf{G} = \left[\frac{\mathcal{B}_1}{r_1} \boldsymbol{\alpha}(\theta_1, \phi_1, r_1), \dots, \frac{\mathcal{B}_K}{r_K} \boldsymbol{\alpha}(\theta_K, \phi_K, r_K)\right], \quad (25)$$

where $\alpha(\theta, \phi, r) = [e^{jk_c d_1}, \dots, e^{jk_c d_N}]^T$, and d_n denotes the distance between the source and the n-th metasurface element, given by

$$d_n = \|\mathbf{p} - \mathbf{t}_n\|$$

$$= \sqrt{r^2 - 2r\sin\theta n_y d - 2r\sin\phi n_z d + n_y^2 d^2 + n_z^2 d^2}.$$
 (26)

When the communication distance falls within the Fresnel region, a second-order Taylor expansion provides a sufficiently accurate approximation for the distance term. In this regime, the distance d_n can be approximated as

$$d_n \approx r - d(\sin\theta n_y + \sin\phi n_z) - \frac{d^2 \sin\theta \sin\phi n_y n_z}{r} + \frac{d^2}{2r} (\cos^2\theta n_y^2 + \cos^2\phi n_z^2).$$
(27)

In the far-field case, where r is typically much larger than the aperture of metasurface, the second-order terms become negligible, and the distance expression simplifies to

$$d_n \approx r - d(\sin\theta n_y + \sin\phi n_z). \tag{28}$$

We define the following parameters:

$$\gamma^{a} = -k_{c}d\sin\theta, \gamma^{e} = -k_{c}d\sin\phi,$$
$$\beta^{e} = \frac{k_{c}d^{2}\cos^{2}\phi}{2r}, \beta^{a} = \frac{k_{c}d^{2}\cos^{2}\theta}{2r}, \alpha = -\frac{k_{c}d^{2}\sin\theta\sin\phi}{r},$$

and substitute them into the distance approximation in (27). This yields the near-field steering vector $\alpha(\theta, \phi, r)$, as expressed in (24). In the far-field regime, the second-order terms vanish, i.e., $\beta^a = \beta^e = \alpha = o(1)$.

By substituting (25) into (11), the received signal can be written as:

$$\mathbf{y} = \mathbf{H}\mathbf{\Phi} \sum_{k=1}^{K} \frac{\epsilon_k}{r_k} \alpha(\theta_k, \phi_k, r_k) s_k + \mathbf{n}, \tag{29}$$

where the channel matrix \mathbf{H} is assumed to be known. Here, we do not consider the design of the decoding matrix \mathbf{F}_{BB} , as we assume that the channel estimation is performed in the radio frequency domain. In the subsequent channel estimation procedure, we first apply a dictionary-based beamspace filtering

$$\alpha(\gamma^{a}, \gamma^{e}, \beta^{a}, \beta^{e}, \alpha) = [e^{j(-N_{h}\gamma^{a} - N_{v}\gamma^{e} + (-N_{h})^{2}\beta^{a} + (-N_{v})^{2}\beta^{e} + (-N_{h})(-N_{v})\alpha)}, \dots, e^{j(-N_{h}\gamma^{a} + N_{v}\gamma^{e} + (-N_{h})^{2}\beta^{a} + N_{v}^{2}\beta^{e} + (-N_{h})N_{v}\alpha)}, e^{j((-N_{h}+1)\gamma^{a} - N_{v}\gamma^{e} + (-N_{h}+1)^{2}\beta^{a} + (-N_{v})^{2}\beta^{e} + (-N_{h}+1)(-N_{v})\alpha)}, \dots, e^{j(N_{h}\gamma^{a} + N_{v}\gamma^{e} + N_{h}^{2}\beta^{a} + N_{v}^{2}\beta^{e} + N_{h}N_{v}\alpha)}]^{\mathsf{T}}e^{jk_{c}r}.$$
(24)

technique (see Section III-A) to obtain a coarse estimation in the angular domain. Based on the coarse angular sets, we then perform refined estimation of angle and distance as described in Section III-B.

A. Coarse estimation

When the channel varies slowly or high estimation accuracy is not strictly required, the rapid phase-switching capability of metasurface can be leveraged to perform full angular space scanning. The core idea is to dynamically configure the phase coefficients of the metasurface across time slots, thereby constructing a measurement function that maps angular directions to received signal energy. We refer to this approach as dictionary-driven beamspace filtering, which combines two core mechanisms: 1) a metasurface-generated beamspace dictionary to sparsify the channel response, and 2) a filtering-inspired reconstruction to extract angular information.

For analytical tractability, we denote the number of sampling points as $T_1 = P \times Q$, where P and Q represent the quantization levels for the azimuth and elevation angles, respectively. During the scanning phase, it is assumed that the symbols transmitted by sources remain constant. At sub-slot $l = p \times q$, the phase shift of the $\tilde{n} = (n_h, n_v)$ -th unit cell is configured to simultaneously compensate for the phase delays toward both the receiving elements and the discretized angular direction (θ_p, ϕ_q) , as given by

$$\omega_{\tilde{n}} = k_c d(\sin \theta_p n_h + \sin \phi_q n_v) + \arg(h_{\tilde{n}})$$

= $\arg(\boldsymbol{\alpha}^*(\theta_p, \phi_q, \infty)) + \arg(h_{\tilde{n}}),$ (30)

where $h_{\tilde{n}} = \text{sum}(\mathbf{H}_{[:,\tilde{n}]})$ denotes the sum of all elements in the \tilde{n} -th column of matrix \mathbf{H} , i.e., $\mathbf{H}_{[:,\tilde{n}]}$ represents the column vector formed by all rows in the \tilde{n} -th column of \mathbf{H} .

Subsequently, the received signals at each sub-slot l are summed to construct the following measurement function:

$$f_l \stackrel{\triangle}{=} \operatorname{sum}(\mathbf{y}_l) = \mathbf{h}^\mathsf{T} \mathbf{\Phi}_l \mathbf{G} \mathbf{s} + \operatorname{sum}(\mathbf{n}_l),$$
 (31)

where $\mathbf{h} = [h_1, \dots, h_N]^\mathsf{T} \in \mathbb{C}^N$ denotes the aggregated metasurface-to-receiver channel. The phase configuration Φ_l at sub-slot l effectively imposes a directional spatial filter, selectively enhancing signal components originating from the beamspace direction (θ_p, ϕ_q) . After T_1 sub-slots, the resulting measurement vector $\mathbf{f} = [f_1, \dots, f_{T_1}]$ exhibits a pronounced peak only when the true angles lie within the sampled grid.

However, due to the absence of strict orthogonality between far-field and near-field steering vectors, the measurement output exhibits a non-sparse energy distribution, where the true angle manifests as a dominant peak accompanied by sidelobe spreading [25]. To obtain a coarse angle estimate, we apply a filtering operation around the main lobe of the observed energy peak. By setting a power attenuation threshold of 3 dB, the angular sets for the estimated azimuth can be expressed as

$$\hat{\mathbf{\Theta}} = \bigcup_{k=1} [\theta_{\text{peak},k} - \Delta\theta_k, \theta_{\text{peak},k} + \Delta\theta_k], \quad (32)$$

where $\Delta \theta_k$ satisfies

$$\Delta \theta_k = \max \left\{ \delta \middle| \mathbf{f}(\theta_{\text{peak},k} \pm \delta) \ge \frac{\mathbf{f}(\theta_{\text{peak},k})}{\sqrt{2}} \right\}.$$
 (33)

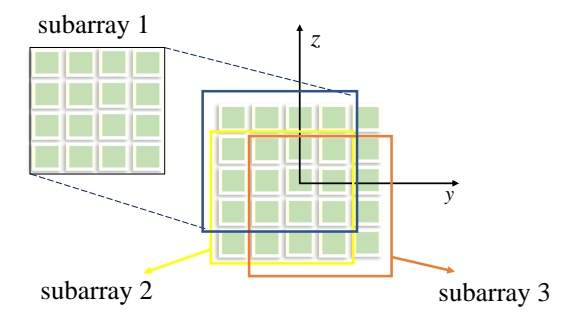


Fig. 5: Spatial subarray partitioning of the metasurface.

Here, the power decay threshold determines the angular resolution of the estimated sets: a larger threshold yields a narrower and more accurate angular interval, while a smaller threshold results in a wider, more conservative estimate.

B. Refined estimation

The coarse estimation in the previous stage significantly reduces the angular search space, enabling the subsequent super-resolution algorithm to accurately estimate both angles and distances. This method relies on estimating the covariance matrix of the channel from the sources to the metasurface. However, since the number of receiver antennas is significantly smaller than the number of metasurface elements, multiple signal stacking is required to obtain a unique estimate of **Gs**.

Assume that T_2 time slots are used for covariance estimation, and each time slot is further divided into S subslots $(S \ge \lfloor \frac{N}{M} \rfloor)$. The metasurface adopts different phase configurations at each sub-slots. By stacking the received signals across sub-slots, we construct the following matrix representation:

$$\tilde{\mathbf{y}} = \tilde{\mathbf{H}}\mathbf{G}\mathbf{s} + \tilde{\mathbf{n}} \in \mathbb{C}^{(M \times S) \times 1},$$
 (34)

where $\tilde{\mathbf{H}} = [\mathbf{H}\boldsymbol{\Phi}_1,\ldots,\mathbf{H}\boldsymbol{\Phi}_S]^\mathsf{T} \in \mathbb{C}^{(M\times S)\times N}$, and $\tilde{\mathbf{n}} = [\mathbf{n}_1,\ldots,\mathbf{n}_S]^\mathsf{T} \in \mathbb{C}^{(M\times S)\times 1}$ denote the effective stacked channel and noise matrices, respectively. Following the procedure in [30], the vector $\mathbf{G}\mathbf{s}$ can be estimated via the least squares (LS) method. Based on this, the sample covariance matrix is computed as

$$\Sigma_s = \frac{1}{T_2} \sum_t \mathbf{G} \mathbf{s}_t (\mathbf{G} \mathbf{s}_t)^{\mathsf{H}} = \mathbf{G} \mathbf{S} \mathbf{G}^{\mathsf{H}} + \sigma^2 (\tilde{\mathbf{H}}^{\mathsf{H}} \tilde{\mathbf{H}})^{-1}, \quad (35)$$

where $\mathbf{S} = \sum_t \mathbf{s}_t \mathbf{s}_t^{\mathsf{H}}/T_2$ denotes the signal power matrix. The eigenvalue decomposition of Σ_s can be expressed as

$$\mathbf{\Sigma}_{s} = \mathbf{U}_{s} \mathbf{\Lambda}_{s} \mathbf{U}_{s}^{\mathsf{H}} + \mathbf{U}_{n} \mathbf{\Lambda}_{n} \mathbf{U}_{n}^{\mathsf{H}},$$

where $\mathbf{U}_s \in \mathbb{C}^{N \times K}$ denotes the signal subspace associated with the K largest eigenvalues, and $\mathbf{U}_n \in \mathbb{C}^{N \times (N-K)}$ is its orthogonal complement representing the noise subspace. The matrices $\mathbf{\Lambda}_s \in \mathbb{C}^{K \times K}$ and $\mathbf{\Lambda}_n \in \mathbb{C}^{(N-K) \times (N-K)}$ are diagonal, containing the corresponding eigenvalues of $\mathbf{\Sigma}_s$.

We partition the metasurface into three subarrays symmetrically distributed with respect to the coordinate origin. Subarray #1 comprises the first $2N_h$ elements along the horizontal (y-axis) and the last $2N_v$ elements along the vertical (z-axis), with coordinate ranges $(-N_h, N_h - 1)$ for the y-axis and

 $(-N_v+1,N_v)$ for the z-axis. Subarray #2 is obtained by shifting subarray #1 downward by one unit along the z-axis, resulting in a coordinate range of $(-N_v,N_v-1)$ in the vertical direction. Similarly, subarray #3 follows the same structure, as shown in 5. Accordingly, the channel matrix corresponding to the *i*-th subarray has the following structure

$$\mathbf{G}_i = [\frac{\mathcal{B}_1}{r_1} \boldsymbol{\alpha}_{N_i}(\theta_1, \phi_1, r_1), \dots, \frac{\mathcal{B}_K}{r_K} \boldsymbol{\alpha}_{N_i}(\theta_K, \phi_K, r_K)],$$

where α_{N_i} denotes the subarray steering vector obtained by extracting a subset of rows from the full array steering vector α . That is, the matrix \mathbf{G}_i is obtained by selecting specific rows from the full channel matrix \mathbf{G} while preserving the original column ordering

$$\mathbf{G}_i = \mathbf{J}_i \mathbf{G} \in \mathbb{C}^{(2N_h \times 2N_v) \times K}, \quad i = 1, 2, 3, \tag{36}$$

where $\mathbf{J}_i \in \mathbb{C}^{(2N_h \times 2N_v) \times N}$ is a binary row-selection matrix. and defined element-wise as

$$[\mathbf{J}_i]_{m,n} = \begin{cases} 1, & n = m + \lceil \frac{m}{2N_v} \rceil + \varrho_i \\ 0, & \text{else} \end{cases}$$
 (37)

For different values of i, we have $\varrho_1=0$, $\varrho_2=-1$ and $\varrho_3=2N_v$. This construction ensures that \mathbf{J}_i acts as a structured selector that extracts specific $(2N_h\times 2N_v)$ rows from the $((2N_h+1)\times (2N_v+1))$ rows of \mathbf{G} .

Define the exchange matrix J as a square matrix with ones on the anti-diagonal and zeros elsewhere. Based on the geometric symmetry between subarray #1 and subarray #3, the following relationship holds

$$\mathbf{J}\boldsymbol{\alpha}_{N_1}(\gamma_k^a,\gamma_k^e,\beta_k^a,\beta_k^e,\alpha_k) = \mathbf{D}(\gamma_k^a,\gamma_k^e)\boldsymbol{\alpha}_{N_3}(\gamma_k^a,\gamma_k^e,\beta_k^a,\beta_k^e,\alpha_k),$$

where

$$\mathbf{D}(\gamma_k^a, \gamma_k^e) = \operatorname{diag}(e^{j2(N_h - 1)\gamma_k^a}, e^{j2(N_h - 2)\gamma_k^a}, \dots, e^{j2(-N_h)\gamma_k^a}) \\ \otimes \operatorname{diag}(e^{j2N_v\gamma_k^e}, e^{j2(N_v - 1)\gamma_k^e}, \dots, e^{j2(-N_v + 1)\gamma_k^e}).$$
(38)

Accordingly, the channel matrices satisfy the following symmetry

$$\mathbf{JG}_{1} = [\mathbf{D}(\gamma_{1}^{a}, \gamma_{1}^{e}) \frac{\epsilon_{1}}{r_{1}} \boldsymbol{\alpha}_{N_{3}} (\gamma_{1}^{a}, \gamma_{1}^{e}, \beta_{1}^{a}, \beta_{1}^{e}, \alpha_{1}), \dots, \mathbf{D}(\gamma_{K}^{a}, \gamma_{K}^{e}) \times \frac{\epsilon_{1}}{r_{1}} \boldsymbol{\alpha}_{N_{3}} (\gamma_{K}^{a}, \gamma_{K}^{e}, \beta_{K}^{a}, \beta_{K}^{e}, \alpha_{K})].$$
(39)

Similarly, we apply the selection matrices J_i to extract the corresponding portions of the signal subspace

$$\mathbf{U}_i = \mathbf{J}_i \mathbf{U}_s, \quad i = 1, \dots, 3,$$

where the signal subspace $\mathbf{U}_s = \mathbf{GT}$ for some full-rank matrix $\mathbf{T} \in \mathbb{C}^{K \times K}$. We now construct the following spectral function to estimate the azimuth and elevation angular components

$$f(\hat{\gamma}^a, \hat{\gamma}^e) = \det(\mathbf{WJU}_1 - \mathbf{WD}(\gamma^a, \gamma^e)\mathbf{U}_3)^{-1}.$$
 (40)

where $\mathbf{W} \in \mathbb{C}^{K \times (2N_h \times 2N_v)}$ is an arbitrary full-rank weighting matrix, and $\mathbf{D}(\hat{\gamma}^a, \hat{\gamma}^e)$ is a parameterized diagonal matrix following the Kronecker structure defined in (38).

It can be observed that when the estimated angular pair $(\hat{\gamma}^a, \hat{\gamma}^e)$ coincides with the true values (γ_k^a, γ_k^e) , the k-th column of the matrix $\mathbf{JG}_1 - \mathbf{D}(\gamma^a, \gamma^e)\mathbf{G}_3$ becomes zero, as

Algorithm 1 Proposed Channel Estimation Algorithm

Input: Arbitrary full-rank matrix **W**, exchange matrix **J** (anti-diagonal ones), received signal **y**

Output: Estimated angular sets $\hat{\Theta}$, $\hat{\Psi}$, and channel parameters $\{\theta, \phi, \mathbf{r}\}$

Stage 1: Coarse Angle Estimation

- 1: **for** t = 1 **to** T_1 **do**
- 2: Configure the phase ω_t according to (30)
- 3: Compute measurement f_t via (31)
- 4: end for
- 5: Aggregate measurements $\mathbf{f} = [f_1, \dots, f_{T_1}]$
- 6: Identify angular sets $\{\hat{\Theta}_i, \hat{\Psi}_i\}_{k=1}^K$ using peak and 3dB region search in (32), (33)

Stage 2: Refined Parameter Estimation

- 7: **for** t = 1 **to** T_2 **do**
- 8: Stack received signals $\{\mathbf{y}_1, \dots, \mathbf{y}_S\}$ into matrix $\tilde{\mathbf{y}}_t$
- 9: end for
- 10: Compute sample covariance matrix as in (35) and obtain signal subspace $\hat{\mathbf{U}}_s$
- 11: Construct subarray selection matrices \mathbf{J}_i and compute $\mathbf{U}_i = \mathbf{J}_i \hat{\mathbf{U}}_s$
- 12: **for** each $(\hat{\theta}_i, \hat{\phi}_i) \in \{\hat{\Theta}_i, \hat{\Psi}_i\}_{k=1}^K$ **do**
- 13: Estimate refined angles $\{\hat{\theta}_k, \hat{\phi}_k\}$ by maximizing the spectral function in (40)
- 14: Substitute estimated angles into (42) and search for \hat{r}_k by maximizing $g(\cdot)$
- **15: end for**

a direct consequence of the subarray symmetry described in (39). This leads to a rank deficiency in the matrix $\mathbf{WJU}_1 - \mathbf{WD}(\gamma^a, \gamma^e)\mathbf{U}_3$. As a result, the directions of DoAs can be estimated by performing a two-dimensional search for the peak of the spectral function $f(\hat{\gamma}^a, \hat{\gamma}^e)$ defined in (40). The estimated azimuth and elevation angles are then given by

$$(\hat{\theta},\hat{\phi}) \!=\! \Big\{ \arcsin(\frac{\hat{\gamma}^a}{k_c d}), \arcsin(\frac{\hat{\gamma}^e}{k_c d}) | (\hat{\gamma}^a\!,\!\hat{\gamma}^e) \!\in\! \arg\max_{\hat{\pmb{\Theta}},\hat{\pmb{\Psi}}} f(\gamma^a\!,\!\gamma^e) \Big\},$$

where $\hat{\Theta}$ and $\hat{\Psi}$ represent the angular sets regions for azimuth and elevation, respectively, which are obtained via the coarse estimation procedure detailed in Section III-A.

Having estimated the source's angular parameters, we now proceed to describe the method for distance estimation. Similar to the angular case, we derive a rotational relationship between the steering vectors associated with subarray #1 and subarray #2, given by

$$\boldsymbol{\alpha}_{N_1}(\gamma_k^a, \gamma_k^e, \beta_k^a, \beta_k^e, \alpha_k) = e^{j\gamma_k^e} \mathbf{E}(\beta_k^e, \alpha_k) \boldsymbol{\alpha}_{N_2}(\gamma_k^a, \gamma_k^e, \beta_k^a, \beta_k^e, \alpha_k),$$

where the diagonal matrix $\mathbf{E}(\beta_k^e, \alpha_k)$ is defined as

$$\mathbf{E}(\beta_k^e, \alpha_k) = \operatorname{diag}(e^{j(-N_h)\alpha_k}, e^{j(-N_h+1)\alpha_k}, \dots, e^{j(N_h-1)\alpha_k}) \\ \otimes \operatorname{diag}(e^{j(-2N_v+1)\beta_k^e}, e^{j(-2N_v+3)\beta_k^e}, \dots, e^{j(2N_v-1)\beta_k^e}).$$

Based on this relationship, we define a spectral function for distance estimation as

$$g(\hat{\beta}^e, \hat{\alpha}) = \det(\mathbf{W}\mathbf{U}_1 - \mathbf{W}\mathbf{E}(\beta^e, \alpha)\mathbf{U}_2)^{-1}.$$
 (41)

Since the angles $(\hat{\theta}_k, \hat{\phi}_k)$ have already been estimated in (40), we traverse the candidate distance values and compute the associated (β_k^e, α_k) to evaluate the above function. The matrix $\mathbf{W}\mathbf{U}_1 - \mathbf{W}\mathbf{E}(\beta^e, \alpha)\mathbf{U}_2$ becomes rank-deficient when $(\hat{\beta}^e, \hat{\alpha})$ matches the true values, thereby indicating the correct distance. Accordingly, the estimated distance \hat{r}_k corresponding to the k-th signal component is obtained by

$$\hat{r}_k \in \arg\max_r g(\beta_k^e, \alpha_k), \tag{42}$$

where the parameters β_k^e and α_k are functions of r and the estimated angles, given by:

$$\beta_k^e = k_c d^2 \cos^2 \hat{\phi}_k / (2r), \alpha_k = -k_c d^2 \sin \hat{\theta}_k \sin \hat{\phi}_k / r.$$

When $\hat{r}_k > 2(D_h^2 + D_v^2)/\lambda$, i.e., beyond the Fresnel distance threshold defined in [33], the corresponding path can be classified as a far-field signal. The proposed algorithm is thus capable of simultaneously estimating the positions and quantities of both near-field and far-field sources. The complete channel estimation procedure is summarized in Algorithm 1. The total number of metasurface sampling points required for channel estimation is given by $(T_1 + T_2 \times S)$.

IV. SPATIAL RESOLUTION OF THE MELA SYSTEMS

In this section, we compare the MELA system with the traditional ELAA system in terms of spatial resolution. The HPBW quantifies the angular width of the main lobe at half of its peak power, serving as a measure of beam concentration and an important indicator of the system's sensing capability. To derive the HPBW expression for the MELA architecture, we model the MELA as a unified transmitter. Accordingly, the previously designated M receiving antennas now operate in transmission mode to illuminate the metasurface.

For the passive metasurface, the resulting radiation field depends on both the incident field and the applied phase shifts. Here, we assume that the metasurface adopts a phase compensation strategy to maximize power transmission. Then, based on the symmetry of the overall channel, the radiated power observed in the far-field outgoing direction (θ_r, ϕ_r) can be expressed as [34]

$$y = \sum_{m=1}^{M} \mathbf{g}^{\mathsf{H}}(\theta_r, \phi_r, \infty) \mathbf{\Phi} \mathbf{h}(\theta_m, \phi_m, r_m), \tag{43}$$

where $g(\theta_r,\phi_r,\infty)=\frac{\mathcal{B}_r}{r_r}\alpha(\theta_r,\phi_r)$ denotes the far-field channel vector with r_r representing the distance in the outgoing direction and \mathcal{B}_r defined in Theorem 1. The vector $\mathbf{h}(\theta_m,\phi_m,r_m)=[\mathbf{H}^{\mathsf{H}}]_{(:,m)}$ corresponds to the m-th column of \mathbf{H}^{H} and represents the near-field channel between the m-th feed antenna and the metasurface. Let

$$\mathbf{c}(\theta_r, \phi_r, \theta_m, \phi_m, r_m) = \sum_{m=1}^{M} \frac{\mathcal{B}_r}{r_r} \boldsymbol{\alpha}(\theta_r, \phi_r) \odot \mathbf{h}(\theta_m, \phi_m, r_m),$$

then (43) can be simplified as $y = \mathbf{c}^{\mathsf{H}}(\theta_r, \phi_r, \theta_m, \phi_m, r_m)\boldsymbol{\omega}$, which is maximized when the phase of metasurface compensates for that of the vector \mathbf{c} , i.e.,

$$\tilde{\omega}_n = \arg([\mathbf{c}(\theta_r, \phi_r, \theta_m, \phi_m, r_m)]_n). \tag{44}$$

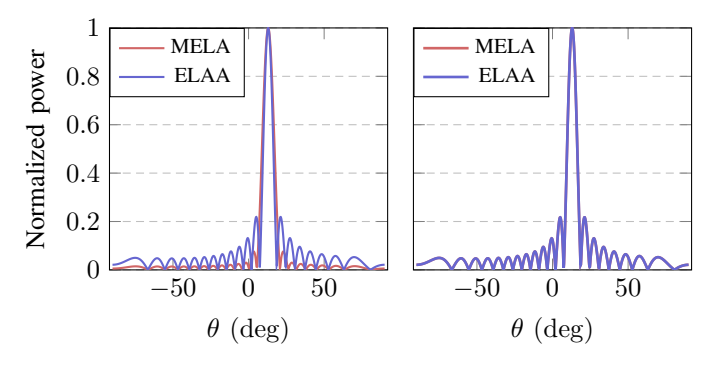


Fig. 6: Normalized array factor power versus azimuth angle. Results in **red** are obtained by (IV) and results in **blue** corresponds to the array factor expression from Formula (16) in [35]. **Left:** Near-field feeds at distances [0.04, 0.05, 0.06]; HPBWs of MELA and ELAA are 9.02° and 6.85°, respectively. **Right:** Far-field feeds at [2.5, 2.6, 2.7]; HPBWs are 7.20° (MELA) and 6.85° (ELAA).

Accordingly, for a given observation direction $(\theta_{\text{out}}, \phi_{\text{out}})$, the array factor is computed as

$$\begin{split} & \text{AF}(\theta_{\text{out}}, \phi_{\text{out}}) = \mathbf{c}^{\mathsf{H}}(\theta_{\text{out}}, \phi_{\text{out}}, \theta_m, \phi_m, r_m) \tilde{\mathbf{w}} \\ &= \frac{\epsilon_r \epsilon_{\text{out}}}{r_r r_{\text{out}}} \boldsymbol{\alpha}^{\mathsf{H}}(\theta_r, \phi_r) \Big(\boldsymbol{\alpha}(\theta_{\text{out}}, \phi_{\text{out}}) \odot \text{mag} \big(\sum_{m=1}^{M} \mathbf{h}(\theta_m, \phi_m, r_m) \big) \Big). \end{split}$$

Half-power beamwidth can be found by determining the half-power point $(\theta_{\rm out},\phi_{\rm out})$ that satisfies

$$20\log(\frac{AF(\theta_{\text{out}},\phi_{\text{out}})}{AF_{\text{max}}}) = -3. \tag{45}$$

As derived from $AF(\theta_{out}, \phi_{out})$, when the feed antennas are located sufficiently far from the metasurface, the following approximation holds

$$\sum_{m=1}^{M} \mathbf{h}(\theta_m, \phi_m, r_m) \approx \sum_{m=1}^{M} \mathcal{A}_m \alpha(\theta_m, \phi_m), \quad (46)$$

where A_m is the channel coefficient corresponding to the m-th column of \mathbf{H} , and is given by

$$\mathcal{A}_m = \frac{I_0 l \eta}{4\pi k_c} \cdot \frac{j(1+\Gamma)d_r^2}{4\pi r_m} \cdot \operatorname{sinc}\left(\frac{k_c v_y d_r}{2}\right) \operatorname{sinc}\left(\frac{k_c v_z d_r}{2}\right),$$

with $v_u = \sin \theta_m \sin \phi_m$ and $v_z = \cos \theta_m$.

In this asymptotic case, the magnitude variation across the elements of $\sum_{m=1}^{M}\mathbf{h}(\theta_m,\phi_m,r_m)$ becomes negligible, and the HPBW of the MELA system closely approximates that of conventional ELAA architectures. Furthermore, when the magnitude of each element in (46) is identical (e.g., when M=1), the phase shifts effectively compensate for the phase differences of the incident waves. In this case, we have

$$\frac{\mathrm{AF}(\theta_{\mathrm{out}},\phi_{\mathrm{out}})}{AF_{\mathrm{max}}} \approx \frac{\sin\Psi_1}{\Psi_1} \cdot \frac{\sin\Psi_2}{\Psi_2},$$

where $\Psi_1 = k_c d(\sin \theta_r - \sin \theta_{\rm out})$ and $\Psi_2 = k_c d(\sin \phi_r - \sin \phi_{\rm out})$. The resulting HPBW expression coincides with that of a conventional antenna array [35].

However, when the feed antennas are placed close to the metasurface, the HPBW expression in (45) becomes dependent on the feed-to-metasurface distance. In this regime, the

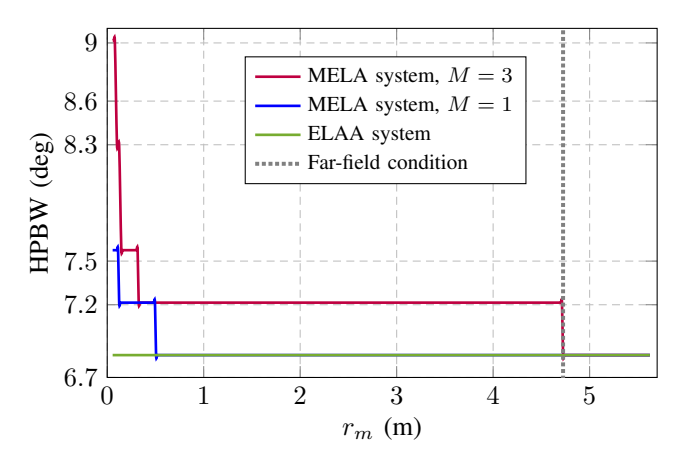


Fig. 7: The HPBW versus the distance r_m . The feed antennas is located at a random angle, with the distance set as $r_m = \sqrt{D_h^2 + D_v^2} \cdot [0.5:0.5:50]$.

weighting coefficients across the array elements vary significantly, resulting in a broader HPBW compared to conventional ELAA systems, as illustrated in Fig. 6 and Fig. 7. In such cases, digital beamforming is required to compensate for the variations in path distance.

V. NUMERICAL RESULTS

In this section, we present numerical simulations to validate the proposed model and algorithms. Assume there are 15 feed antennas and a metasurface with 21×21 elements. The system operates at a carrier frequency of 28 GHz, and the elements are spaced at half-wavelength intervals. In Section V-A, we analyze the impact of various system parameters on the proposed electromagnetic channel model. Subsequently, in Section V-B, we validate the effectiveness of the proposed beamspace filtering method and compare our channel estimation algorithm with with two other hybrid-domain estimation techniques and the Cramér–Rao bound (CRB).

A. Impact of System Parameters on the channel

Consider a scenario where three single-dipole sources transmit uplink signals, and the receiver is equipped with a uniform linear array with element spacing equal to one wavelength. Both the metasurface elements and the receiving antenna elements are assumed to have a size of $d_r = d_t = \frac{\lambda}{2}$. We define the normalized correlation coefficient based on the received signals as $\rho_{(\cdot)} = |\mathbf{y}_{(\cdot)}^{\mathsf{H}} \mathbf{y}_{\mathsf{true}}|^2 / (|\mathbf{y}_{(\cdot)}|^2 |\mathbf{y}_{\mathsf{true}}|^2),$ which serves to quantify the correlation between different approximate models and the accurate electromagnetic model. Fig. 8 illustrates the correlation coefficients between the true values and the approximate model, the decoupled model, and the linear model, under varying placement distances, by substituting (9), (19), and (23) into (11). It is observed that the approximate electromagnetic model closely matches the true field, serving as an upper bound in terms of the correlation coefficient. When the metasurface-receiver distance exceeds the decoupling distance, the decoupled model also exhibits strong agreement with the true model, as indicated by a beam power value approaching 1. Furthermore, once the distance

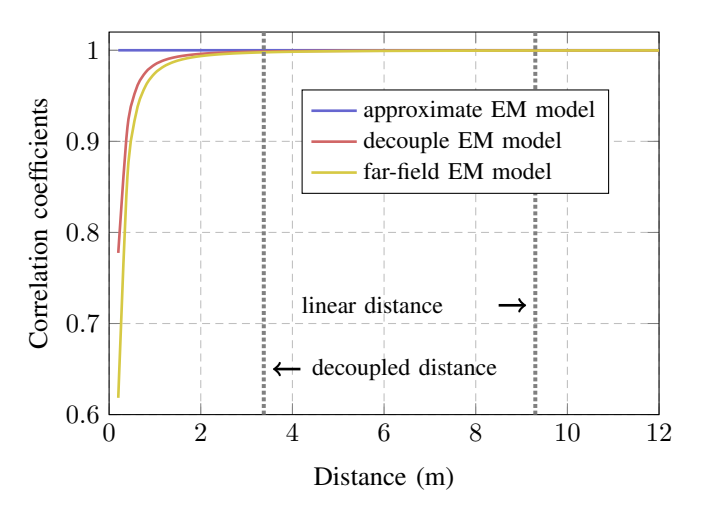


Fig. 8: The correlation coefficients versus the distance between the geometric center of metasurface and receiver.

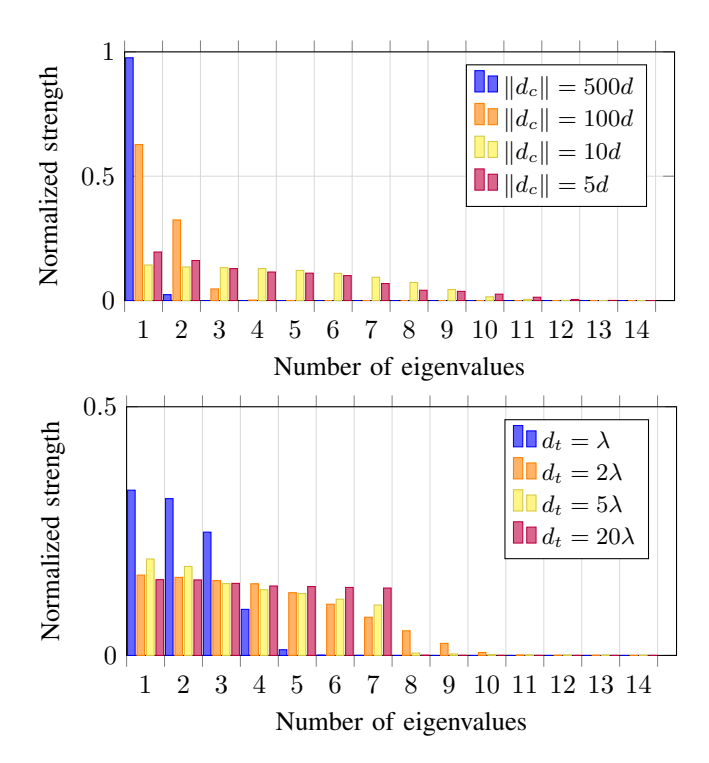


Fig. 9: The distribution of the normalized eigenvalue strength under different parameter settings. **Top:** The eigenvalues of **H** in decreasing order with element size $d_r = d_t = \lambda/2$. **Bottom:** The eigenvalues of **H** in decreasing order with TRIS-receiver distance $d_c = 10\lambda$. d_r is set as $d_r = d_t$.

surpasses the linear distance, the beam power curves of the linear, decoupled, and electromagnetic models converge, demonstrating their consistency in the far-field regime.

In Fig. 9, we examine the impact of physical parameters on the degrees of freedom (DoF) of the metasurface–receiver channel in the near-field scenario. A higher DoF implies that the channel can support a greater number of independent data streams at a given signal-to-noise ratio (SNR). We present in Fig. 9 the variations in the eigenvalue distribution of **H**

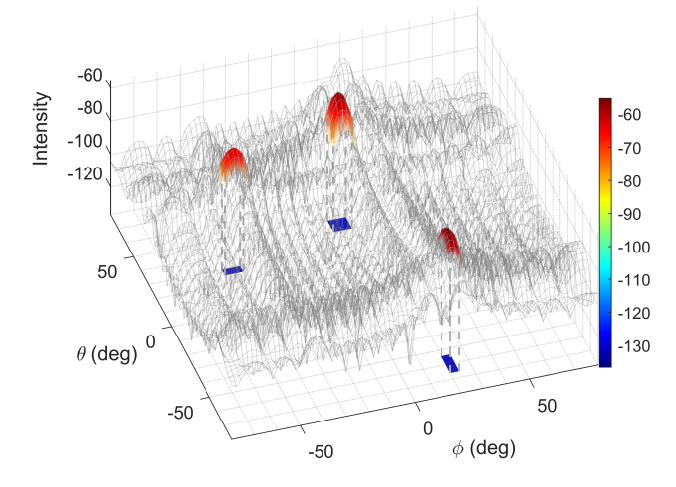


Fig. 10: The distribution of the measurement equation in the angular space.

with respect to the metasurface–receiver center distance d_c , as well as the element sizes of the transmissive unit cell d_t and the receiving antenna d_r . It is observed that the DoF of the channel decreases as d_c increases, which manifests as rank deficiency in the channel matrix, where a few dominant eigenvalues emerge while the remaining ones diminish. Meanwhile, increasing the element size and thereby enlarging the antenna aperture leads to a higher DoF.

B. Channel Estimation

To validate the effectiveness of the beamspace filtering method introduced in Section III-A, we perform a full-space scan over both azimuth and elevation angles ranging from -90° to 90° . Three sources are assumed to be located at $(-59.5^{\circ}, 21.4^{\circ})$, $(44.4^{\circ}, 8.1^{\circ})$, and $(28.7^{\circ}, -43.3^{\circ})$. The energy attenuation threshold is set to 3 dB, the SNR is -5 dB, and all other parameters are consistent with those used in Fig. 8. The resulting measurement function is shown in Fig. 10, where the spatial quantization level is set as P = Q = 40. As illustrated in the figure, the observation function exhibits a clear peak at the true signal locations. The angular sets, coarsely estimated via beamspace filtering, corresponds to the angle regions within the 3 dB amplitude attenuation threshold, highlighted in red.

In Fig. 11, we further investigate the impact of system parameters, including the power attenuation threshold and the number of scan samples. To rigorously quantify the estimation accuracy, we introduce a weighted score metric, defined as follows

score =
$$\rho \cdot \bar{L} + (1 - \rho) \cdot MSE_a$$
.

Here, \bar{L} denotes the average width of the estimated angular interval, ρ is a weighting parameter that balances the trade-off between interval width and estimation bias, and MSE_a represents the mean squared error of angle estimation. Evidently, a larger power attenuation threshold leads to coarser yet more stable estimates, increasing the likelihood that the true angle lies within the estimated interval. In contrast, a smaller threshold may result in narrower intervals that exclude the

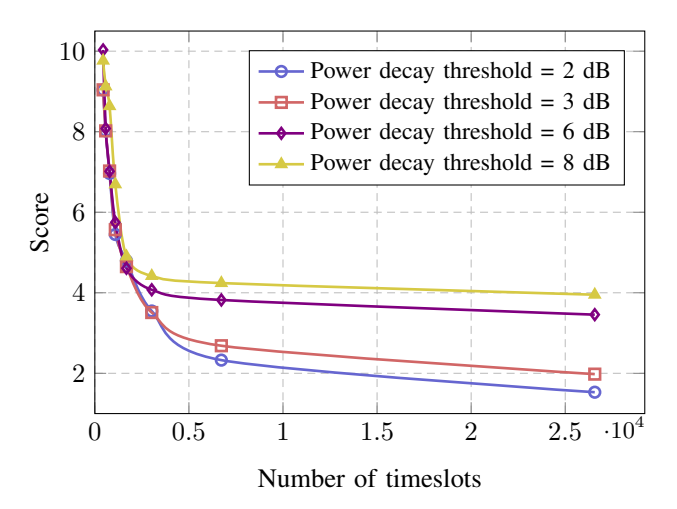


Fig. 11: The weighted score versus the number of sample spaces under different power decay thresholds. The SNR is set to -5 dB. Results are averaged over 500 independent trials.

true angle, thereby degrading the performance of subsequent fine channel estimation. Additionally, a larger scan sample size requires more pilot symbols and incurs higher computational complexity. The results in Fig. 11 further demonstrate that when channel remain stable over an extended pilot duration, a power attenuation threshold of 3 dB (corresponding to the performance curve's inflection point) and a scan range of $[-90^\circ\!:\!2^\circ\!:\!90^\circ]$ can be optimally selected as the system configuration. Beyond this setting, further increasing the sample size or reducing the power attenuation threshold yields marginal performance improvement.

Based on the possible angular setss obtained in Section V-B, Fig. 12 illustrates the variation of the estimation MSE of the proposed refined algorithm with respect to both the SNR and the number of samples T_2 . The number of sources is set to K = 3, each time slot is divided into S = 30sub-slots, and the phase configuration of the metasurface is randomized in each sub-slot. Two scenarios are considered: a hybrid far-near-field case with two far-field and one nearfield signals, and another case where all three sources are in the near field. The results show that the estimation MSE for both angles and distances decreases as the SNR increases, with the most significant improvement observed when the SNR exceeds -5 dB. Notably, the MSE of angular estimation for $T_2 = 100$ closely approaches that for $T_2 = 500$, whereas the MSE of distance estimation at $T_2 = 100$ still exhibits a noticeable gap compared to the $T_2 = 500$ case. These results confirm the robustness of the proposed algorithm across both hybrid and pure near-field scenarios, as indicated by the nearly overlapping MSE curves for these two scenarios.

C. Comparison to other approaches

In this section, we compare the proposed channel estimation algorithm with two benchmark methods: the modified MUSIC algorithm introduced in [31] and the hybrid-field orthogonal matching pursuit (HF-OMP) approach proposed in [27].

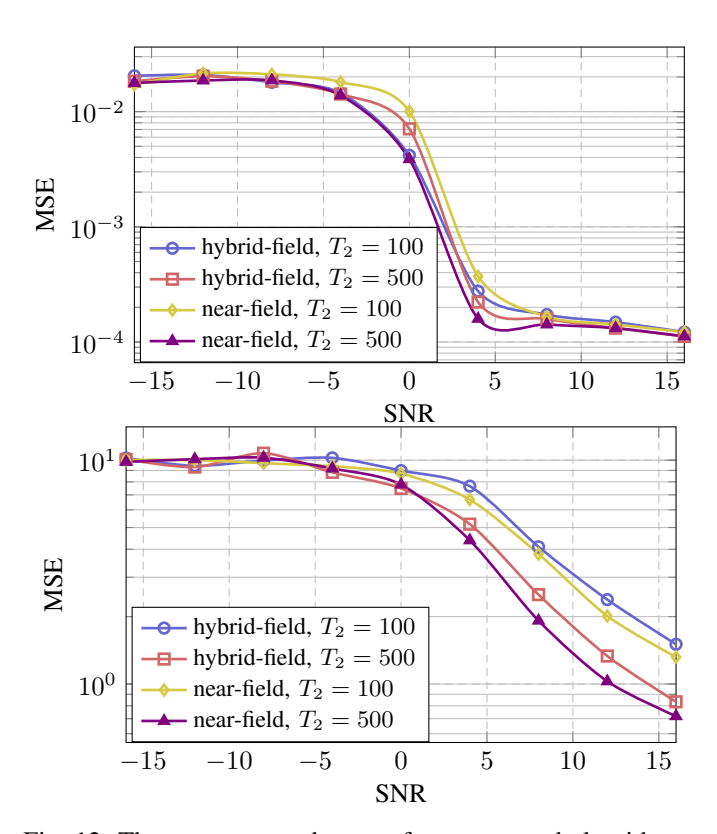


Fig. 12: The mean squared error of our proposed algorithm varies with the SNR under different number of time slots. Top: MSE in the angular domain. Bottom: MSE in the distance domain.

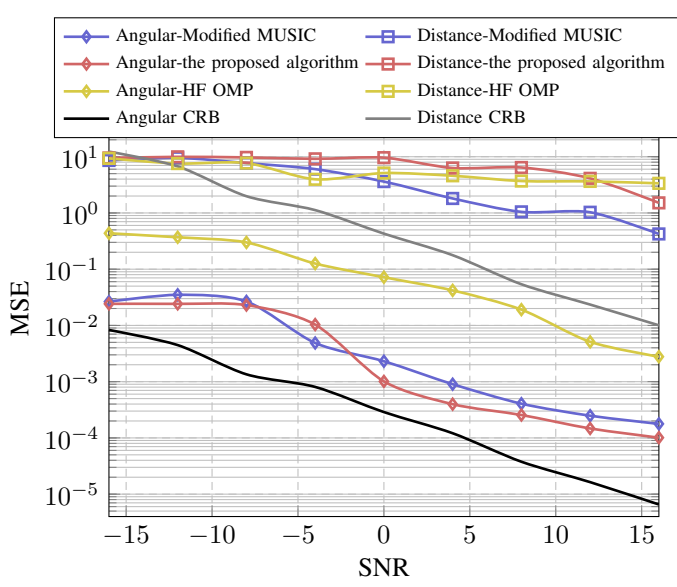


Fig. 13: The MSE versus SNR. The SNR is set to -5 dB. Results are averaged over 500 independent trials.

For the modified MUSIC implementation, spatial smoothing is performed by partitioning the metasurface into 144 subarrays, each with a dimension of 10×10 . The simulation is conducted under the hybrid-field scenario with K=3 signals and $T_2 = 100$ time samples, while all other parameters are consistent with those in Fig. 12. The CRB curve is computed following the method in [36]. As shown in Fig. 13, the

proposed algorithm outperforms both benchmarks in terms of MSE. The performance of the HF-OMP algorithm is limited by the lack of orthogonality among atoms in its polar-domain dictionary, which degrades its resolution capability compared to the other super-resolution algorithms. The modified MUSIC algorithm, while effective, exhibits higher MSE compared to the proposed method because it employs a approximated near-field model that neglects second-order terms [37]. This limitation is explicitly accounted for in our proposed modeling framework.

VI. CONCLUSION

In this paper, we have proposed a low-hardware-complexity solution for ELAA systems: a transceiver architecture that combines a minimal set of active antennas with a metasurface, referred to as MELA. We have derived a physically interpretable and mathematically tractable channel model for this architecture, which lavs the foundation for system performance analysis and algorithm design. To support efficient channel acquisition, we have designed a two-stage estimation scheme: a coarse angular scanning stage to identify candidate directions, followed by a refinement stage that jointly estimates angles and ranges by leveraging sub-array symmetry. Furthermore, our derived HPBW formula for the MELA architecture demonstrates that the system can achieve spatial resolution performance comparable to conventional ELAA systems with equivalent antenna configurations. This near-optimal resolution performance highlights the potential of MELA, while also motivating further exploration of digital precoding, which are not considered in this work. Future research directions include hybrid beamforming design for MELA transceivers.

APPENDIX A PROOF OF THEOREM 1

The vector $\frac{\mathbf{d}_{mn}}{|\mathbf{d}_{mn}|} - \frac{\mathbf{p} - \mathbf{t}_n}{|\mathbf{p} - \mathbf{t}_n|}$ represents the directional difference between the path from the n-th transmissive unit cell to the m-th receiving antenna and the path from the n-th unit cell to the source located at p_k . Since the receiving antennas are typically located within a compact region, the variation in the normalized direction vector $\mathbf{d}_{mn}/|\mathbf{d}_{mn}|$ across antennas is negligible. Therefore, we approximate all receiving antennas by their geometric center, i.e., $\mathbf{d}_{mn} \approx \mathbf{d}_{cn}$. Define the direction mismatch vector as:

$$\mathbf{u} = \mathbf{d}_{cn} / \|\mathbf{d}_{cn}\| - \mathbf{p}_k - \mathbf{t}_n / \|\mathbf{p}_k - \mathbf{t}_n\| = [u_x, u_y, u_z].$$

Given that the transmissive unit cell spans a square region with local coordinates $\Delta \mathbf{t}_y, \Delta \mathbf{t}_z \in [-d_r/2, d_r/2]$, the surface integral of the phase term factorizes as

$$\iint_{-d_r/2}^{d_r/2} e^{jk_c \mathbf{u}^\mathsf{T} \Delta \mathbf{t}_n} d\Delta t_y d\Delta t_z \qquad (47)$$

$$= \int_{-d_r/2}^{d_r/2} e^{jk_c u_y \Delta t_y} d\Delta t_y \times \int_{-d_r/2}^{d_r/2} e^{jk_c u_z \Delta t_z} d\Delta t_z, \quad (48)$$

$$= \int_{-d_r/2}^{d_r/2} e^{jk_c u_y \, \Delta t_y} \, d\Delta t_y \, \times \, \int_{-d_r/2}^{d_r/2} e^{jk_c u_z \, \Delta t_z} \, d\Delta t_z, \tag{48}$$

Each one-dimensional integral is elementary:

$$\int_{-d_r/2}^{d_r/2} e^{jk_c u_y \, \Delta t_y} \, d\Delta t_y = \frac{2 \, \sin\left(\frac{k_c u_y d_r}{2}\right)}{k_c u_y}, \tag{49}$$

and similarly $\int_{-d_r/2}^{d_r/2} e^{jk_c u_z \, \Delta t_z} \, d\Delta t_z = 2 \, \sin \left(\frac{k_c u_z d_r}{2} \right) / (k_c u_z)$. Therefore, the overall result is

$$\int_{S_{\star}} e^{jk_c \mathbf{u}^{\mathsf{T}} \Delta \mathbf{t}_n} d\Delta \mathbf{t}_n = \frac{2 \sin\left(\frac{k_c u_y d_r}{2}\right)}{k_c u_y} \times \frac{2 \sin\left(\frac{k_c u_z d_r}{2}\right)}{k_c u_z}.$$

REFERENCES

- [1] Weiqiang Tan, Dongqing Xie, Junjuan Xia, Weijie Tan, Lisheng Fan, and Shi Jin, "Spectral and energy efficiency of massive mimo for hybrid architectures based on phase shifters," *IEEE Access*, vol. 6, pp. 11751–11759, 2018.
- [2] Roi Méndez-Rial, Cristian Rusu, Nuria González-Prelcic, Ahmed Alkhateeb, and Robert W. Heath, "Hybrid mimo architectures for millimeter wave communications: Phase shifters or switches?," *IEEE Access*, vol. 4, pp. 247–267, 2016.
- [3] Zhe Wang, Jiayi Zhang, Hongyang Du, Dusit Niyato, Shuguang Cui, Bo Ai, Mérouane Debbah, Khaled B. Letaief, and H. Vincent Poor, "A tutorial on extremely large-scale mimo for 6G: Fundamentals, signal processing, and applications," *IEEE Communications Surveys & Tutorials*, vol. 26, no. 3, pp. 1560–1605, 2024.
- [4] Zhe Wang, Jiayi Zhang, Hongyang Du, Wei El Sha, Bo Ai, Dusit Niyato, and Mérouane Debbah, "Extremely large-scale mimo: Fundamentals, challenges, solutions, and future directions," *IEEE Wireless Commun.*, vol. 31, no. 3, pp. 117–124, 2023.
- [5] Hongkang Yu, Yuan Si, Shujuan Zhang, and Yijian Chen, "Patterned beam training: A novel low-complexity and low-overhead scheme for elaa," 2024.
- [6] Yiling Yuan, Chao Wang, Chao Li, Zhimeng Zhong, Wei Han, and Cheng-Xiang Wang, "Spatial correlations of measured mimo channels with an extremely large aperture array (elaa)," in 2022 IEEE 95th Vehicular Technology Conference: (VTC2022-Spring), 2022, pp. 1–5.
- [7] Sicong Ye, Ming Xiao, Man-Wai Kwan, Zheng Ma, Yongming Huang, George Karagiannidis, and Pingzhi Fan, "Extremely large aperture array (elaa) communications: Foundations, research advances and challenges," *IEEE Open J. Commun. Soc.*, vol. 5, pp. 7075–7120, 2024.
- [8] Ming Xiao, Shahid Mumtaz, Yongming Huang, Linglong Dai, Yonghui Li, Michail Matthaiou, George K Karagiannidis, Emil Björnson, Kai Yang, Amitabha Ghosh, et al., "Millimeter wave communications for future mobile networks," *IEEE J. Sel. Areas Commun.*, vol. 35, no. 9, pp. 1909–1935, 2017.
- [9] Roi Méndez-Rial, Cristian Rusu, Nuria González-Prelcic, Ahmed Alkhateeb, and Robert W Heath, "Hybrid mimo architectures for millimeter wave communications: Phase shifters or switches?," *IEEE access*, vol. 4, pp. 247–267, 2016.
- [10] Yu Han, Shi Jin, Michail Matthaiou, Tony QS Quek, and Chao-Kai Wen, "Toward extra large-scale mimo: New channel properties and low-cost designs," *IEEE Internet Things J.*, vol. 10, no. 16, pp. 14569–14594, 2023
- [11] Mengzhen Liu, Ming Li, Rang Liu, and Qian Liu, "Dynamic hybrid beamforming designs for ELAA near-field communications," *IEEE Journal on Selected Areas in Communications*, vol. 43, no. 3, pp. 644–658, 2025.
- [12] Shuhao Zeng, Hongliang Zhang, Boya Di, Yunhua Tan, Zhu Han, H. Vincent Poor, and Lingyang Song, "Reconfigurable intelligent surfaces in 6g: Reflective, transmissive, or both?," *IEEE Commun. Lett.*, vol. 25, no. 6, pp. 2063–2067, 2021.
- [13] D. McGrath, "Planar three-dimensional constrained lenses," *IEEE Trans. Antennas Propag.*, vol. 34, no. 1, pp. 46–50, 1986.
- [14] Antonio Clemente, Laurent Dussopt, Ronan Sauleau, Patrick Potier, and Philippe Pouliguen, "Focal distance reduction of transmit-array antennas using multiple feeds," *IEEE Antennas Wirel. Propag. Lett.*, vol. 11, pp. 1311–1314, 2012.
- [15] Luca Di Palma, Antonio Clemente, Laurent Dussopt, Ronan Sauleau, Patrick Potier, and Philippe Pouliguen, "Radiation pattern synthesis for monopulse radar applications with a reconfigurable transmitarray antenna," *IEEE Trans. Antennas Propag.*, vol. 64, no. 9, pp. 4148–4154, 2016
- [16] Zheng Xing Wang, Jun Wei Wu, Han Qing Yang, Qun Yan Zhou, Si Ran Wang, Hui Xu, Li Jie Wu, Yinghui Quan, Qiang Cheng, and Tie Jun Cui, "A hybrid architecture for programmable meta-system using a few active elements," *Laser & Photonics Reviews*, vol. 18, no. 8, pp. 2400062, 2024.
- [17] Zhendong Li, Wen Chen, and Huanqing Cao, "Beamforming design and power allocation for transmissive rms-based transmitter architectures," *IEEE Wireless Commun. Lett.*, vol. 11, no. 1, pp. 53–57, 2021.

- [18] Bojiang Li, Wen Chen, Zhendong Li, Qingqing Wu, Nan Cheng, Changle Li, and Linglong Dai, "Robust weighted sum-rate maximization for transmissive ris transmitter enabled rsma networks," *IEEE Commun. Lett.*, vol. 27, no. 10, pp. 2847–2851, 2023.
- [19] Zhendong Li, Wen Chen, Xusheng Zhu, Qingqing Wu, Gang Ni, Shan-shan Zhang, and Jun Li, "Transmissive ris transceiver enabled multi-stream communication systems: Design, optimization and analysis," *IEEE Internet Things J.*, 2024.
- [20] Zhendong Li, Wen Chen, Qingqing Wu, Ziwei Liu, Chong He, Xudong Bai, and Jun Li, "Transmissive ris enabled transceiver systems: Architecture, design issues and opportunities," arXiv preprint arXiv:2408.13483, 2024.
- [21] Zhendong Li, Wen Chen, Qingqing Wu, Xusheng Zhu, Haoran Qin, Kunlun Wang, and Jun Li, "Toward transmissive ris transceiver enabled uplink communication systems: Design and optimization," *IEEE Internet Things J.*, vol. 11, no. 4, pp. 6788–6801, 2023.
- [22] Özlem Tuğfe Demir and Emil Björnson, "User-centric cell-free massive mimo with ris-integrated antenna arrays," in 2024 IEEE 25th International Workshop on Signal Processing Advances in Wireless Communications (SPAWC). Ieee, 2024, pp. 546–550.
- [23] Chong Han, Yuhang Chen, Longfei Yan, Zhi Chen, and Linglong Dai, "Cross far-and near-field wireless communications in terahertz ultralarge antenna array systems," *IEEE Wireless Commun.*, 2024.
- [24] Xun Wu, Changsheng You, Jiapeng Li, and Yunpu Zhang, "Near-field beam training: Joint angle and range estimation with dft codebook," *IEEE Trans. Wireless Commun.*, 2024.
- [25] Shaohua Yue, Shuhao Zeng, Liang Liu, Yonina C. Eldar, and Boya Di, "Hybrid near-far field channel estimation for holographic mimo communications," *IEEE Transactions on Wireless Communications*, vol. 23, no. 11, pp. 15798–15813, 2024.
- [26] Mingyao Cui and Linglong Dai, "Channel estimation for extremely large-scale mimo: Far-field or near-field?," *IEEE Trans. Commun.*, vol. 70, no. 4, pp. 2663–2677, 2022.
- [27] Xiuhong Wei and Linglong Dai, "Channel estimation for extremely large-scale massive mimo: Far-field, near-field, or hybrid-field?," *IEEE Commun. Lett.*, vol. 26, no. 1, pp. 177–181, 2021.
- [28] Hongwei Wang, Jun Fang, and Jilin Wang, "Compressive near/far-field channel estimation for mmwave/thz systems with extremely large antenna arrays," in GLOBECOM 2023-2023 IEEE Global Communications Conference. IEEE, 2023, pp. 2354–2359.
- [29] Yang Xi, Fuqiang Zhu, Binggui Zhou, Ting Liu, and Shaodan Ma, "Gridless hybrid-field channel estimation for extra-large aperture array massive mimo systems," *IEEE Wireless Commun. Lett.*, vol. 13, no. 2, pp. 496–500, 2023.
- [30] Parisa Ramezani, Alva Kosasih, and Emil Björnson, "An efficient modified music algorithm for ris-assisted near-field localization," arXiv preprint arXiv:2409.14152, 2024.
- [31] Jin He, MNS Swamy, and M Omair Ahmad, "Efficient application of music algorithm under the coexistence of far-field and near-field sources," *IEEE Trans. Signal Process.*, vol. 60, no. 4, pp. 2066–2070, 2011.
- [32] Antoine Le Calvez, Luc Le Magoarou, and Stéphane Paquelet, "Massive mimo channel estimation taking into account spherical waves," arXiv preprint arXiv:1811.05669, 2018.
- [33] Weidong Li, Haifan Yin, Ziao Qin, and Mérouane Debbah, "Wavefront transformation-based near-field channel prediction for extremely large antenna array with mobility," *IEEE Trans. Wireless Commun.*, vol. 23, no. 10, pp. 15613–15626, 2024.
- [34] Constantine A Balanis, Antenna theory: analysis and design, John wiley & sons, 2016.
- [35] Rujing Xiong, Jialong Lu, Jianan Zhang, Minggang Liu, Xuehui Dong, Tiebin Mi, and Robert Caiming Qiu, "Design and optimization on successive ris-assisted multi-hop wireless communications," arXiv preprint arXiv:2407.10080, 2024.
- [36] Jingxuan Zhou, Yinchao Yang, Zhaohui Yang, and Mohammad Reza Shikh-Bahaei, "Near-field extremely large-scale star-ris enabled integrated sensing and communications," *IIEEE Trans. Green Commun.* Netw., vol. 9, no. 1, pp. 404–416, 2025.
- [37] Wei Huang, Cuiling Li, Yong Zeng, Caihong Kai, and Shiwen He, "Near-field full dimensional beam codebook design for xl-mimo communications," in GLOBECOM 2023-2023 IEEE Global Communications Conference. IEEE, 2023, pp. 4902–4908.